1 **Preprint**

2

3 **EntireAxon: Deep learning deciphers four distinct patterns of axonal**

4 **degeneration**

5

6

7 **Alex Palumbo**[1,2,3,*] (ORCID: 0000-0002-1631-785X)**, Philipp Grüning**[4] (ORCID: 0000-0003-

8 2946-4020)**, Svenja Kim Landt**[1,2] (ORCID: 0000-0002-4133-7035), **Lara Eleen Heckmann**[1,2]

9 (ORCID: 0000-0003-1264-9715)**, Luisa Bartram**[1]**, Alessa Pabst**[1,2] (ORCID: 0000-0003-1938-

10 3753)**, Charlotte Flory**[1,2] (ORCID: 0000-0001-5049-6380)**, Maulana Ikhsan**[1,2,3] (ORCID: 0000-

11 0002-8756-4524)**, Sören Pietsch**[1,2,5]**, Reinhard Schulz**[6]**, Christopher Kren**[7]**, Norbert Koop**[7]**,

12 **Johannes Boltze**[1,2,8] (ORCID: 0000-0003-3956-4164**, Amir Madany Mamlouk**[4] (ORCID: 0000-

13 0001-9709-1620) **and Marietta Zille**[1,2,3,*] (ORCID: 0000-0002-0609-8956)

14

15 [1] Fraunhofer Research Institution for Marine Biotechnology and Cell Technology, Lübeck, Germany

16 [2] Institute for Medical and Marine Biotechnology, University of Lübeck, Lübeck, Germany

17 [3] Institute for Experimental and Clinical Pharmacology and Toxicology, University of Lübeck, Lübeck, Germany

18 [4] Institute for Neuro- and Bioinformatics, University of Lübeck, Lübeck, Germany

19 [5] Department of Neonatology, Universitätsklinikum Leipzig, Leipzig, Germany

20 [6] Wissenschaftliche Werkstätten, University of Lübeck, Lübeck, Germany

21 [7] Medical Laser Center Lübeck GmbH, Lübeck, Germany

22 [8] School of Life Sciences, The University of Warwick, Gibbet Hill Campus, Coventry, United Kingdom

23 [*] Correspondance to: alex.palumbo@uni-luebeck.de; m.zille@uni-luebeck.de

24

Abstract

Different axonal degeneration (AxD) patterns have been described depending on the biological condition. Until now, it remains unclear whether they are restricted to one specific condition or can occur concomitantly. Here, we present a novel microfluidic device in combination with a deep learning tool, the EntireAxon, for the high-throughput analysis of AxD. We evaluated the progression of AxD in an *in vitro* model of hemorrhagic stroke and observed that axonal swellings preceded axon fragmentation. We further identified four distinct morphological patterns of AxD (granular, retraction, swelling, and transport degeneration) that occur concomitantly. These findings indicate a morphological heterogeneity of AxD under pathophysiologic conditions. The newly developed microfluidic device along with the EntireAxon deep learning tool enable the systematic analysis of AxD but also unravel a so far unknown intricacy in which AxD can occur in a disease context.

Introduction

40   Axonal degeneration (AxD) is a process in which axons disintegrate physiologically during

41   nervous system development and aging, or as a pathological element of degenerative nervous

42   system diseases[1–3]. During development and neural circuit assembly, inappropriately grown

43   axons can undergo axonal retraction, axonal shedding or local AxD[4,5]. Axonal retraction is

44   characterized by retraction bulb formation at the distal tip, and subsequent pullback[4]. During

45   axonal shedding, the axon sheds small vesicles, called axosomes[6]. Local AxD is characterized

46   by axon disintegration into separated axonal fragments[5].

47   Acutely and chronically injured axons may degenerate retrogradely (dying-back mechanism),

48   anterogradely or in a Wallerian degeneration pattern, ultimately resulting in the generation of

49   axonal fragments[7–9]. Another morphological feature that occurs during AxD in development

50   and disease is axon swelling. The swollen axon contains disorganized cytoskeleton and

51   organelles resulting from an interruption of axonal transport, reactive oxygen species exposure

52   or nutrient deprivation[8,10,11]. Both axonal swellings and axonal fragments represent hallmarks

53   of AxD independent of the biological context[2,12,13]. Therefore, it is relevant to detect the

54   different degeneration patterns and to ascertain their underlying morphological changes to

55   better understand their role in AxD during development and pathophysiology.

56   To assess the spatiotemporal progression of the different AxD patterns, morphological changes

57   of axons must be recorded continuously. However, available software fails to automatically

58   detect and quantify high axon numbers and the morphological features of AxD (swellings and

59   fragments). The reason may be two-fold: 1) Available software relies on image binarization[14,15],

60   which can lead to information loss and low sensitivity as thin axons may not be recognized. 2)

61   The analysis requires subjective and time-consuming manual annotations, e.g., thresholding

62   and defining the region of interest[16–18]. So far, immunostained images were used to investigate

63   morphological changes in AxD as the analysis of phase-contrast images has been limited by the

64   lower target-to-background signal. Immunofluorescence images, however, entail certain

65 disadvantages such as photobleaching and the requirement for cell fixation, which allows only

66 to observe a single time point. Hence, a software tool for the automatized detection and

67 quantification of the morphological patterns of AxD in long-term live cell imaging is required

68 to improve the sensitivity and throughput, which will overcome current limitations in

69 understanding AxD.

70 In this study, we hypothesized that axons can undergo different AxD patterns, which rely on

71 different underlying morphological features and depend on the severity of AxD. To

72 systematically study AxD in a high-throughput manner, we fabricated a microfluidic device in

73 the format of a conventional cell culture plate containing 16 independent microfluidic units that

74 separate axons from their somata. We also developed a novel deep learning tool called

75 "EntireAxon" to analyze AxD in phase-contrast time-lapse recordings. Our newly developed

76 detection algorithm can sensitively and specifically recognize axons, axonal swellings and

77 axonal fragments during AxD in an *in vitro* model of hemorrhagic stroke and its performance

78 is equal to human expert rating. EntireAxon enabled the identification of four different

79 morphological patterns of AxD based on a histogram analysis of segmentation changes over

80 time. These patterns occurred concomitantly and in a concentration-dependent manner in

81 hemin-induced AxD.

Results

A novel microfluidic device for the high-throughput analysis of axonal degeneration

Experimental models such as microfluidic devices have been developed to spatially separate axons from their somata[19,20]. Thus, the axons can be treated in an isolated manner to investigate AxD. The major limiting factor of commercially available microfluidic devices is that they are single, individual systems and hence, can only be used to assess one condition, which is time-consuming and precludes high-throughput analyses.

To overcome this limitation, we manufactured a microfluidic device containing 16 individual microfluidic units by using the soft lithography technique replica molding (**Fig. 1, suppl. Fig. 1**). The spatial separation of axons from their somata was confirmed by immunostaining (**Fig. 1c**) using the established dendritic marker MAP2 and axonal marker synaptophysin[21,22].

The EntireAxon convolutional neural network (CNN) recognizes axons and the morphological features of AxD

To enable the systematic high-throughput analysis of AxD over time in phase-contrast microscopy, we trained the EntireAxon CNN to segment all relevant features of AxD, i.e. axons, axonal swellings, and axonal fragments (**Fig. 2**).

Specifically, we adapted a standard u-net with ResNet-50 encoder[23,24] and used a CNN ensemble, which combines predictions from multiple CNNs to generate a final output and is superior to individual CNNs[25–27]. To validate the training success, a separate labeled validation set unknown to the EntireAxon was created (ground truth was labeled by human expert 1). While the EntireAxon CNN recognized the class 'background' better than the three axon classes 'axon', 'axonal swelling', and 'axonal fragment' (mean F1 score: 0.995), axon-specific segmentation revealed the highest mean F1 score for the class 'axon' (0.780), followed by the classes 'axonal swelling' (0.567), and 'axonal fragment' (0.301) (**Fig. 3a**). The comparably

108   lower performance of the CNN to recognize axonal fragments may be explained by the

109   disproportional distribution of pixels in the training data with a mean of 96.42 % of pixels

110   belonging to the class 'background', while only 2.77% represented the class 'axon', 0.58%

111   'axonal swelling', and 0.23 % 'axonal fragment'.

112   Next, we compared the performance of the trained EntireAxon CNN on the ground truth

113   (human expert 1) with the performance of two additional human experts. The EntireAxon CNN

114   reached higher mean F1 scores for all classes, except for the class 'axonal fragment', where

115   human expert 2 outperformed the EntireAxon CNN (**Fig. 3b**). This may have been due to the

116   fact that the EntireAxon CNN was trained on images labeled by the same human expert (1) that

117   labeled the ground truth. To assess whether its performance is more generalizable across the

118   different experts, we compared the EntireAxon CNN to each of the human experts on the

119   consensus labels of the two other human experts (**Fig. 3c-d**). Visual inspection of the labels

120   showed a wide overlap between the different experts, but also that there was considerable

121   uncertainty, especially for the classification of axonal fragments (**Fig. 3c**). When comparing the

122   mean F1 scores for all classes, the EntireAxon reached similar or even higher scores than the

123   other three experts (**Fig. 3d**). Collectively, this suggests that the EntireAxon CNN sensitively

124   and specifically recognizes axons and the morphological features of AxD, i.e. axonal swellings

125   and axonal fragments.

126

127   **AxD progresses concentration- and time-dependent**

128   We then applied the EntireAxon CNN to assess AxD in an *in vitro* model of hemorrhagic

129   stroke[28]. Accordingly, axons were exposed to the hemolysis product hemin and recorded by

130   time-lapse microscopy for 24 hours. Hemin induced concentration- and time-dependent

131   morphological changes leading to AxD compared to vehicle-treated axons (**Fig. 4 and suppl.**

132   **Videos 1-4**). Area under the curve (AUC) analyses revealed a significant decrease in axon area

133   in all three hemin concentrations (50 µM vs. 0 µM: p=0.026; 100 µM vs. 0 µM: p=0.018,

134   200 µM vs. 0 µM: p<0.001). The axonal swelling area also increased in all three concentrations

135   (50 µM vs. 0 µM: p=0.012, 100 µM vs. 0 µM: p=0.005, 200 µM vs. 0 µM: p=0.016), while the

136   axonal fragment area was elevated only for axons treated with 100 and 200 µM hemin (vs.

137   0 µM: p=0.004, **suppl. Fig. 2**).

138   Comparing the time course of AxD between hemin- and vehicle-treated axons (0 µM), the axon

139   area decreased starting at 11.5 hours at 200 µM (p=0.020, from 15 hours onwards p<0.001), at

140   14 hours at 100 µM (p=0.040, from 18.5 hours onwards p<0.001), and at 15 hours at 50 µM

141   (p=0.018, from 19 hours onwards p<0.001). Hemin treatment also an elevated axonal fragment

142   area starting at 9 hours at 200 µM (p=0.037) and at 17 hours at 100 µM hemin (p=0.044).

143   Interestingly, the axonal swelling area increased prior to the changes in axon and axonal

144   fragment area, i.e. starting at 6 hours at 200 µM (p=0.010) and 100 µM (p=0.019), and at

145   8 hours at 50 µM hemin (p=0.030). For the highest hemin concentration, the increase was only

146   transient (until 18.5 hours), suggesting that axonal swellings preceded the fragmentation of the

147   axon.

148   The results of the time course analysis were further substantiated by live cell fluorescent

149   staining (calcein AM), which indicated the starting point of AxD after hemin treatment between

150   8 and 12 hours for 200 µM hemin, between 12 and 16 hours for 100 µM hemin and 16 and

151   20 hours for 50 µM hemin (**suppl. Fig. 3**). Taken together, the EntireAxon CNN was able to

152   quantify the degree of AxD and to determine the underlying temporal progression.

153

154   **The EntireAxon recurrent neural network (RNN) recognizes four distinct patterns of**

155   **AxD**

156   AxD time series data revealed that different morphological patterns of degeneration can occur

157   in the same axons over time (**Fig. 5** and **suppl. Videos 5-8**). We therefore classified the

158   following four morphological patterns of AxD based on the time-lapse recordings:

159   i) Granular degeneration: AxD resulting in granular separated fragments.

7

160   ii) Retraction degeneration: AxD in which the distal part of the axon retracts ultimately

161   resulting in granular degeneration.

162   iii) Swelling degeneration: AxD with the enlargement of axonal swellings and subsequent

163   granular degeneration.

164   iv) Transport degeneration: AxD in which axonal swellings of constant size, which do not

165   enlarge, are transported along the axon resulting in granular degeneration.

166 We hypothesized that the different morphological AxD patterns can occur concomitantly. We

167 therefore trained the EntireAxon RNN to identify changes in class segregation over time using

168 a training dataset of AxD segmentation recordings (**Fig. 6a**). For each time point, the RNN

169 computed the probability of a change in class for each pixel of an image relative to the previous

170 time point.

171 Based on the 16 different possible class changes, the RNN determined seven clusters (cluster

172 0-6) that were characterized by an idiosyncratic segmentation pattern over 24 hours (**Suppl.**

173 **Fig. 4**). All clusters showed a decrease in the class 'axon' and an increase in the class

174 'background', although to different degrees, temporal patterns, and some of them with

175 concomitant increases in either the class 'axonal swelling' and/or 'axonal fragment'. In cluster

176 0, there was an early decrease in the class 'axon', which then continued more linearly as well

177 as a later rise in the class 'axonal fragment'. In contrast to cluster 0, cluster 1 showed no increase

178 in the class 'axonal fragment' and a linear decrease in the class 'axon' from the start. In cluster

179 2, there was a strong increase in the class 'axonal swelling'. Cluster 3 demonstrated an early

180 and lasting high level of the class 'axonal swelling' with a later increase in the class 'axonal

181 fragment'. Cluster 4 showed a rapid decrease in the class 'axon' concomitant with an increase

182 in the classes 'background' and 'axonal swelling'. Cluster 5 was similar to cluster 1, but with

183 an early drop in the class 'axon'. Cluster 6 showed an increase in the class 'axonal swelling'

184 similar to but to a greater extent than cluster 2.

185   The RNN categorized each cluster to one of the four morphological patterns (**Fig. 6b**): i)

186   Granular degeneration was defined by clusters that describe the degeneration of axons into

187   axonal fragments, i.e. clusters 0, 1, 3, and 5. ii) Retraction degeneration only included the

188   clusters 1 and 5, indicating the retraction of the axon followed by its fragmentation. iii) Swelling

189   degeneration was characterized by the three clusters that included the class 'axonal swelling,

190   i.e. clusters 2, 3, and 6, as well as cluster 5 showing the exchange of the class 'axon' for

191   'background'. iv) Transport degeneration was the only pattern that relied on cluster 4 and was

192   also characterized partly on clusters 0, 1, 2, and 6. Although some clusters overlap among

193   morphological patterns, the unique combination of the different clusters allows to distinguish

194   all four morphological patterns.

195   To validate the EntireAxon RNN, a 10-fold cross-validation was performed, which

196   demonstrated its ability to distinguish between the four morphological patterns of AxD (**Fig.**

197   **6c**). These data confirm that the combination of the different AxD features as well as their

198   spatiotemporal progression defines distinct morphological AxD patterns.

199

200   **The morphological patterns of AxD depend on the extent of AxD**

201   We then applied the EntireAxon RNN to quantify the occurrence of the different morphological

202   patterns of AxD (**Fig. 7**). Hemin-treated axons underwent granular, retraction, swelling, and

203   transport degeneration concomitantly as these patterns occur either close to or at the exact same

204   locations (**Fig. 7a**). Hemin concentration-dependently increased all morphological AxD

205   patterns, with granular degeneration being significantly increased for the 100 µM (p=0.004)

206   and 200 µM hemin samples (p=0.001), while swelling degeneration was significantly increased

207   for 50 µM (p=0.006) and 100 µM (p=0.004) hemin-treated compared to vehicle-treated axons.

208   Neither retraction nor transport degeneration differed among the investigated concentration

209   (**Fig. 7b**).

210   Collectively, our data suggest that hemin gradually shifts the morphological pattern of AxD

211   from swelling degeneration to granular degeneration, which is in accordance with our findings

212   that axonal swellings preceded axonal fragmentation.

Discussion

213

214 We here describe for the first time the concomitant occurrence of four different morphological

215 patterns of AxD under pathophysiological conditions, i.e. granular, retraction, swelling, and

216 transport degeneration. These rely on time- and concentration-dependent changes of the

217 morphological features of AxD, with axonal swellings preceding axon fragmentation. The

218 herein introduced complementary tools consisting of a novel microfluidic device and the

219 EntireAxon deep learning platform allow to increase the experimental yield and the in-depth

220 high-throughput analysis of AxD.

221

222 The extent of AxD has been mainly investigated with a focus on axon fragmentation so far. To

223 quantify axon fragmentation, Sasaki and colleagues introduced the AxD index as the ratio of

224 fragmented axon area versus total axonal area[14]. However, the AxD index did not include

225 axonal swellings, which is another characteristic feature of degenerating axons[11,29]. Hence, the

226 precise spatiotemporal role of axonal swellings in AxD remains elusive.

227 The herein presented EntireAxon CNN performs an automatic segmentation and quantification

228 of axons and morphological features relevant to AxD, including axonal swellings and

229 fragments, on phase-contrast time-lapse microscopy images (**Fig. 2**). The EntireAxon CNN

230 recognized the four classes 'background', 'axon', 'axonal swelling', and 'axonal fragment',

231 with the highest mean F1 score for the class 'background' (**Fig. 3a**) as background pixels

232 covered most of the image.

233 Although the performance of the EntireAxon CNN on the axon-related classes was comparably

234 lower due to the imbalanced prevalence of each class in the images, the comparison with human

235 experts revealed that the EntireAxon CNN reached a similar performance level. As expected,

236 its performance was slightly better than the human experts on the ground truth as both, ground

237 truth and training data, were labeled by the same human expert (**Fig. 3b**). Interestingly, when

238 comparing the EntireAxon CNN with a human expert on the consensus label of the other two

11

239   human experts, not only was the EntireAxon CNN as good as or even better than the human

240   expert, but the mean F1 scores were also higher than on the ground truth labels (**Fig. 3d**). This

241   may be because pixels that were differentially assigned by the human expert, i.e. more difficult

242   to classify, were excluded from the comparison. Taken together, these findings demonstrate

243   that the EntireAxon CNN is suitable to quantify automatically and in a high-throughput manner

244   AxD and its accompanying morphological changes.

245   Using the newly developed EntireAxon CNN, we were able to investigate AxD in an *in vitro*

246   model of hemorrhagic stroke. To our knowledge, this is the first *in vitro* study to characterize

247   AxD after hemorrhagic stroke. AxD is an active and commonly observed process in

248   intracerebral hemorrhage[30,31], with larger hematomas being associated with a more severe

249   progression of white matter injury resulting in poor motor and functional recovery[30,32]. As the

250   underlying mechanisms of AxD in hemorrhagic stroke remain to be elucidated and represent a

251   research priority in the field[33], we investigated the morphological changes that can occur in

252   axons in response to hemorrhage.

253   We therefore modeled hemorrhagic stroke by exposing outgrown axons from primary cortical

254   neurons to the hemolysis product hemin. In our model, AxD started within 12 to 18 hours after

255   the administration of hemin (**Fig. 4** and **suppl. Fig. 3**). Similar AxD starting time points have

256   been observed *in vitro* in other models. For instance, under circumstances of growth factor

257   withdrawal, axons undergo AxD at 12-24 hours[11,34,35].

258   We further demonstrated that the relative axon area decreased with increasing hemin

259   concentrations, while the axonal fragment area increased. Our results are in accordance with

260   other experimental conditions such as axotomy-mediated or paclitaxel-induced AxD, in which

261   the axonal fragments also increased[14,36]. As the axonal swelling area preceded the increase of

262   axonal fragments and axon area loss, our findings are also in line with results reported in a

263   model of experimental autoimmune encephalomyelitis indicating that axonal swelling

264   anticipates fragmentation[10].

265 Interestingly, axonal swellings and axonal fragments were related to different morphological

266 patterns of AxD in our model. Specifically, we observed axons that showed signs of axonal

267 retraction, enlarging of axonal swellings and axonal transport before degeneration (**Fig. 5**).

268 These findings led to the hypothesis that different morphological patterns of AxD can occur

269 concomitantly and should therefore be detectable based on our segmentation data. We therefore

270 trained the EntireAxon RNN to quantify the occurrence of granular, retraction, swelling, and

271 transport degeneration based on the clusters of unique changes of classes over time (**Fig. 6** and

272 **suppl. Fig.4**):

273 i) Granular degeneration has previously been observed in retrograde, anterograde, Wallerian

274 and local AxD[5,7–9]. ii) Retraction degeneration has been described in axonal retraction and

275 shedding[4,6]. iii) Swelling degeneration was previously reported in experimental autoimmune

276 encephalitis and growth factor deprivation[10,11]. iv) In contrast, transport degeneration has not

277 been reported before. However, microtubule breaks have been demonstrated in an *in vitro*

278 model of axonal stretch injury. Those developed into axonal swellings resulting in axonal

279 transport interruption with AxD as a consequence[37]. The underlying molecular mechanisms of

280 the different patterns of AxD need to be further investigated, which could be greatly facilitated

281 by the EntireAxon RNN that is able to automatically detect the different morphological patterns

282 in time-lapse recording due to its capacity to relate each output to previous images in the stacks

283 by its current units.

284 All four patterns occurred concomitantly in hemin-induced AxD (**Fig. 7**), which may point to

285 a potential synergy of the different patterns of AxD. Interestingly, we also observed a

286 concentration-dependent effect, whereat swelling degeneration was significantly increased at

287 lower hemin concentrations while granular degeneration occurred more frequently at higher

288 hemin concentrations. This is in line with our data suggesting that axonal swellings precede

289 axon fragmentation. To what extent our model of hemin-induced AxD in hemorrhagic stroke

13

290   is molecularly similar to developmental or pathophysiological AxD needs to be further

291   investigated.

292   To compare different experimental conditions of AxD, we herein propose a novel monolithic

293   microfluidic device consisting of 16 individual microfluidic units that enable the parallel and

294   separated treatment and/or manipulation of axons and somata (**Fig. 1**). The currently available

295   microfluidic devices do not allow high-throughput experiments as they comprise only single

296   microfluidic units[20,38]. Although some devices can harbor multiple experimental conditions,

297   they employ a radial design where a single soma compartment is used, in which influence from

298   one experimental condition to another experimental condition cannot be excluded due to the

299   potential of retrograde signaling[39,40]. Another option is the parallel use of multiple individual

300   devices, which allows to handle up to 12 devices in a conventional 12-well plate[18]. Compared

301   to our microfluidic device, this procedure is time-consuming in both the manufacturing process

302   and the adjustment for recordings.

303

Limitations and outlook

305   i) Our microfluidic device currently does not allow to investigate AxD at more proximal axonal

306   parts to the soma such as the axonal initial segment. Since intracerebral hemorrhage often

307   occurs in deep brain regions, affecting axons of near-by neurons as well as more distal axonal

308   trajectories, comparing AxD in distal and proximal axonal regions may be of interest.

309   Shortening the length of the microgrooves or including a more proximal compartment, are

310   possible modifications of the current design.

311   ii) Our results are based on unmyelinated axons. Therefore, the time course and morphological

312   changes may be different in co-culture with oligodendrocytes. This warrants possible future

313   investigations.

314   iii) The observed effects of AxD in hemorrhagic stroke within this study were based on hemin

315   toxicity, and we cannot exclude that other hemolysis products such as thrombin or bilirubin

14

316   have different effects. Additional studies should investigate differences of hemolysis products

317   to increase our understanding of the mechanisms of AxD in hemorrhagic stroke.

318   iv) The overall CNN performance may be further improved with more general inputs. For

319   example, the segmentation of fragment pixels cannot be done accurately from a single image

320   at a specific time point as the whole process of AxD, ultimately resulting in the disintegration

321   of the axons (i.e. the generation of axonal fragments), needs to be considered. CNNs using 3D

322   convolutions could, in principle, perform a segmentation over an entire time-lapse recording

323   and model temporal dependencies. However, we decided against the 3D approach, as it severely

324   restricts general applicability due to its greatly increased effort to label suitable time series for

325   training. In this context, the identification of the images that will yield the best results is crucial

326   to effectively reduce labeling costs, which we have previously described using an active

327   learning method[41].

328

329   **Conclusion**

330   Taken together, our approach enables the systematic investigation of AxD in a high-throughput

331   manner. In combination with the microfluidic device, the EntireAxon expands our possibilities

332   to track AxD by detecting axons, axonal swellings and axonal fragments and identifying the

333   related different morphological patterns of AxD. This will help to tackle the complex processes

334   of AxD and may significantly enhance our understanding of AxD in health and disease. It may

335   also support the development of novel treatment approaches for neurodegenerative diseases.

336

Online methods

Chemicals and reagents are listed in the **supplementary information (suppl. Tables 4-5)**.

Fabrication of a high-throughput microfluidic device based on soft lithographic replica molding

Thirty-two wells were milled in a polymethyl methacrylate (PMMA) plate of the size of a conventional cell culture plate (**Fig. 1, suppl. Fig. 1**) using a universal milling machine (Mikron WF21C, Mikron Holding AG) with a 1 mm triple tooth cutter (HSS-CO8 Type N, Holex) at a precision of 0.01 mm. During the milling procedure, we applied a half-synthetic cooling lubricant (Opta Cool 600 HS, Wisura GmbH) on a mineral base to reduce the amount of debris. Additionally, we milled screw holes in the intermediate spaces between each microfluidic unit to later detach the PMMA from the negative casting mold. To remove debris, we washed the PMMA plate by sonication (Sonicator Elmasonic S, Elma Schmidbauer GmbH) at room temperature for 30 minutes. Next, we lasered the microgrooves on the PMMA plate to connect both milled compartments of each individual microfluidic unit by using an Excimerlaser (Excistar XS 193 nm, Coherent). The PMMA plate was then washed again by sonication at room temperature for 30 minutes.

Polydimethylsiloxane (PDMS) was prepared in a 1:10 ratio and mixed properly before inducing vacuum at 0.5 Torr in a vacuum desiccator (Jeio Tech VDC-31) for 30 minutes. After the PDMS was poured into an empty aluminum basin to cover the ground, we applied vacuum at 0.5 Torr for 30 minutes to remove air bubbles. The PDMS was cured at room temperature for 48 hours. We put the PMMA plate on top of the PDMS ground with the milled and lasered structures showing upwards. Half of each well of the microfluidic units was filled with PDMS before curing at room temperature for 48 hours. We mixed the epoxy solution in a 1:1 ratio and poured it over the microfluidic device to cover its surface by at least 1 cm. Vacuum was applied at 0.5

363   Torr for 10 minutes to remove all air bubbles located above the channel side of the microfluidic

364   device. The epoxy was cured at room temperature for a minimum of 2 hours. We subsequently

365   detached the epoxy from the PMMA plate via a metallic block that consisted of screw holes in

366   the intermediate spaces between the individual systems. The epoxy represented a negative

367   casting mold to produce the microfluidic devices using PDMS.

368   PDMS was prepared as described above. We poured the PDMS into the negative epoxy casting

369   mold and applied vacuum at 0.5 Torr for 30 minutes. The liquid PDMS was cured at 75 °C for

370   2 hours to induce the polymerization. We peeled the microfluidic devices from the casting mold

371   and punched the wells with an 8 mm biopsy punch (DocCheck Shop GmbH) to ensure a

372   sufficient amount of medium for cell culture. We cleaned customized 115 x 78 x 1 mm glass

373   slides by sonication (Sonicator Elmasonic S, Elma Schmidbauer GmbH) and subsequently

374   cleaned them by ethanol before plasma treatment (High Power Expanded Plasma Cleaner,

375   Harrick Plasma). Plasma was applied at 45 W and 0.5 Torr for 2 minutes to activate the silanol

376   groups of the glass slides and the microfluidic devices enabling firm attachment.

377   We washed the microfluidic devices with ethanol and then twice with distilled water to remove

378   any debris. After aspirating the distilled water, except from the inside of the compartments,

379   0.1 mg/mL of poly-d-lysine solution (PDL) in 0.02 M borate buffer (0.25 % (w/v) borate acid,

380   0.38 % (w/v) sodium tetraborate in distilled water, pH 8.5) was used for coating at 4 °C

381   overnight. We aspirated the PDL the next morning, not removing it from the compartments,

382   and added 50 µg/mL of laminin as a second coating surface for incubation at 4 °C overnight.

383   At the day of neuron isolation, the microfluidic devices were washed twice with pre-warmed

384   medium after aspirating the laminin. Immediately prior to cell seeding, we aspirated the

385   medium from the wells without removing it from the compartments.

386

387   **Experimental animals**

388   Crl:CD1 (ICR) Swiss outbred mice (Charles River) were used. The animals were kept at 20-

389   22 °C, 30-70 % humidity in a 12-hour/12-hour light/dark cycle and were fed a normal chow

390   diet (Altromin Spezialfutter GmbH) *ad libitum*. Animal experiments followed the protocol of

391   the "NIH Guide for the care and use of laboratory animals" and were approved by the

392   Schleswig-Holstein Ministry for Energy Transition, Agriculture, Environment, Nature and

393   Digitalization (under the prospective contingent animal license number 2017-07-06 Zille).

394

395   **Isolation and culture of primary cortical neurons**

396   We isolated primary cortical neurons (PCNs) from murine E14 embryos after decapitation as

397   previously described[28]. We seeded the PCNs at a density of 10,000 cells/mm^2 in 5 µL

398   MEM+Glutamax medium into one compartment (soma compartment) of each microfluidic unit

399   of the device. The cells adhered at 37 °C for 30 minutes. In order to promote the growth of the

400   axons in one direction into the other compartment (axonal compartment) by medium microflux,

401   150 µL of MEM+Glutamax medium were applied to the well of the soma compartment, while

402   100 µL were added to the well of the axonal compartment. PCNs were cultured at 37 °C in a

403   humidified 5 % CO_2 atmosphere. We changed from MEM+Glutamax medium to Neurobasal

404   Plus Medium containing 2 % B-27 Plus Supplement, 1 mM sodium pyruvate and 1 %

405   penicillin/streptomycin at day-in vitro (DIV) 1. The volume differences among the wells

406   ensured the microflux for the directional axonal growth over the following days.

407

408   **Immunofluorescence**

409   Soma and axonal compartments in the microfluidic units were fixed at room temperature for

410   1 hour in 4 % formaldehyde solution in PBS. They were washed twice with PBS and

411   permeabilized with blocking solution (2 % BSA, 0.5% Triton-X-100 and 1x PBS) at room

412   temperature for 1 hour. We incubated the neurons/axons on both compartments with primary

413   antibodies against synaptophysin (1:250) and MAP2 (1:4000) at 4 °C overnight. The next day,

414   both compartments were washed three times with PBS and incubated with the secondary

415   antibodies anti-mouse Alexa Fluor 546 (1:500) and anti-rabbit Alexa Fluor 488 (1:500) at room

416   temperature for 1 hour. After washing three times with PBS, both compartments were incubated

417   with DAPI (1 µg/mL) for nuclear counterstaining at room temperature for 10 minutes. Both

418   compartments were finally washed three times with PBS prior to fluorescence microscopy.

419

420   **Selection of microfluidic units for hemin treatment and time-lapse recording**

421   At DIV 6 or 7, microfluidic devices were considered for recording if they met the following

422   inclusion criteria: i) axon growth through at least 80 % of all microgrooves and ii) axon length

423   of at least 150 µm from the end of the microgrooves. Microfluidic units were randomly assigned

424   to experimental conditions.

425

426   **Time-lapse recording of axonal degeneration**

427   Microfluidic units were randomly selected and axons were treated with 0 (vehicle), 50, 100,

428   and 200 µM hemin. For the treatment, the media was removed from the wells of the

429   microfluidic units; hemin was diluted in the collected media and added back to the respective

430   wells. The media volume between the two wells was equalized during the treatment to prevent

431   any microflux. We started the recordings at 1 hour after treatment to allow for the adjustment

432   of the well plates to the humidity of the incubation chamber of the microscope and the setup of

433   the recording positions. We recorded AxD with a 30-minutes interval for 24 hours using an

434   Olympus IX81 time-lapse microscope (Olympus Deutschland GmbH) with a 10X objective

435   (0.3 NA Ph1) at 37 °C, 5 % CO_2 and 65 % humidity.

436

437   **Live cell fluorescent staining**

19

438   To evaluate axonal vitality, we washed the axonal compartment once with PBS and incubated

439   the axonal compartment with calcein AM (4 µM) for 30 minutes at 37 °C at the end of the time-

440   lapse recording or in 4-hour intervals upon hemin treatment.

441

442   **Training of the EntireAxon CNN for the segmentation of phase-contrast microscopic**

443   **images**

444   We trained the EntireAxon CNN for the image-wise semantic segmentation of AxD features.

445   To this end, we adapted a standard u-net with ResNet-50 encoder[23] to automatically determine

446   the class probability for each pixel of an input image. Our segmentation aimed to classify each

447   pixel of a microscopic image of a time-lapse recording into one of four classes: 'background',

448   'axon', 'axonal swelling', and 'axonal fragment'.

449   For the training dataset, we selected 33 images and created corresponding image labels (masks)

450   using GIMP (v.2.10.14, RRID:SCR_003182). For each image, a label image with the same

451   height and width was created, in which each pixel value denotes a pixel class. Specifically, the

452   classes 'background', 'axon', 'axonal swelling', and 'axonal fragment' had the values 0, 1, 2,

453   and 3, respectively. For each pixel of the input image, we retained 4 values that are the

454   probability distribution of the pixel over the 4 classes. To create a segmentation map, we

455   assigned each pixel the most probable class. During training, the CNN observed an input image,

456   produced an output and compared this output to the label. Via backpropagation, the weights of

457   the network were adapted so that the output better fitted the label. The pixelwise loss function,

458   from which the weight changes were derived, was the cross-entropy loss:

459    $$Loss(P, Y) \ = \ -\sum_{x,y,c} Y(x, y, c) \ log(P(x, y, c));$$

460   With $P(x, y, c) \ and \ Y(x, y, c)$ being the probability of class c at pixel (x, y) for the prediction

461   and ground truth of the network, respectively.

462

463   We trained a mean ensemble consisting of eight neural networks for 180 epochs using the Adam

464   optimizer, a batch size of four and a learning rate of 0.001 that decreased by a factor of ten after

465   every 60 epochs. The input images were standardized by the image-net mean and standard

466   deviation [42]. For data augmentation, we used random cropping (size 512 x 512), image flipping

467   along the horizontal axis and rotation by a random angle between -90° and +90°.

468

469   **Validation of the EntireAxon CNN compared to human experts**

470   To measure how well the EntireAxon CNN segments unknown images, we used a second

471   validation set comprising eight images that were labeled by three human experts. Importantly,

472   the EntireAxon CNN did not update its parameters during training to fit the validation set, but

473   only used the training set.

474   For each image, the EntireAxon CNN inferred a segmentation. We generated a binary mask

475   from the prediction of the network, where 1 denotes the respective class and 0 all other classes.

476   We computed a binary label mask in the same manner. We counted the true positive (TP), false

477   positive (FP), and false negative (FN) pixels and computed the recall (sensitivity) and

478   precision[43]:

479
$$Recall = \frac{TP}{TP + FN}$$

480
$$Precision = \frac{TP}{TP + FP}$$

481   Recall and precision were calculated for each class separately on each validation image. The

482   mean recall and precision over all eight validation images was determined subsequently.

483   A mean of 96.42 % of pixels in the axonal images were 'background' pixels, while only 2.77 %

484   represented the class 'axon', 0.58 % 'axonal swelling', and 0.23 % 'axonal fragment' pixels.

485   This reflects a challenging degree of class imbalance, where the probability of having any

486   positives for a class in a validation image is low. Thus, we did not use the computed recall and

487   precision of the individual images or the mean recall and precision to compute the mean F1

488   score, i.e. the harmonic mean of recall and precision. This has been shown to lead to bias,

489   especially when a high degree of class imbalance is present in the dataset[43] as it may result in

490   undefined values for an image for recall (due to the absence of TP), precision (in case the CNN

491   does not recognize the few positives), and F1 score (in case either recall or precision are

492   undefined). To avoid bias, we computed the total TP, FP, and FN of all validation images from

493   which we calculated the mean F1 score[43]:

494

$$mean\ F1\ score = \frac{2 * TP_{total}}{2 * TP_{total} + FP_{total} + FN_{total}}$$

495   In addition, we computed a consensus label between human expert 1 and 2, 1 and 3 as well as

496   2 and 3 and compared the EntireAxon CNN versus the remaining expert (human expert 3, 2,

497   and 1, respectively) to the consensus labels. Mean F1 scores for all classes were computed as

498   described above.

499

500   **Image preprocessing**

501   Prior to the analysis of AxD after hemin exposure, we preprocessed the time-lapse recordings

502   in ImageJ (v1.52a, RRID: RRID:SCR_003070) using a custom-written macro. Specifically,

503   each individual recording was converted from a 16-bit into an 8-bit recording to make it

504   compatible with the ImageNet (8-bit) pre-trained ResNet-50. The recording was aligned

505   automatically with the ImageJ plug-in "Linear Stack Alignment with SIFT" as described

506   previously[44]. The following settings were used: initial Gaussian blur of 1.6 pixel, 3 steps per

507   scale octave, minimum image size of 64 pixel, maximum image size of 1024 pixel, feature

508   descriptor size of 4, 8 feature descriptor orientation bins, closest/next closest ratio of 0.92,

509   maximal alignment error of 25 pixel; inlier ratio of 0.05, expected transformation as rigid,

510   "interpolate" and "show info" checked. Black edges appearing on the recording after alignment

511   were cropped.

512

AxD analysis using the EntireAxon CNN

All recordings of AxD after hemin exposure were automatically analyzed by the trained EntireAxon CNN, which classified each pixel as one of the four different classes 'background', 'axon', 'axonal swelling', and 'axonal fragment. For each experimental condition (i.e. hemin concentration), the sum percentage of all pixels per class on all images of that experimental day were added at each time point ('Axon$_{t1.5-24h}$, Axonal swelling$_{t1.5-24h}$, Axonal fragment$_{t1.5-24h}$). To determine the changes for the classes 'axon', 'axonal swelling', and 'axonal fragment' over time, we calculated the sum percentage of pixels for all given time points (t_i with i = 1.5 to 24 hours) of the corresponding class over the sum of the pixels of all three classes at baseline:

$$normalized\ 'class'\ area\ (t_i)$$

$$= \frac{'Class'_{ti}}{Axon_{t1.5h} + Axonalswelling_{t1.5h} + Axonalfragments_{t1.5h}} * 100$$

Classification of the morphological patterns of AxD using attention-based RNN

We used the segmentation videos to identify four morphological patterns of AxD: i) granular, ii) retraction, iii) swelling, and iv) transport degeneration. To reduce the dimensions of the input, each frame was converted into a histogram. To compute a histogram for a frame t_i, we compared the pixels of the frames t_i and t_{i+1}. Each pixel was assigned into one of 16 classes that consisted of the pairwise tuples $(c_1, c_2) \in \{0,1,2,3\}^2$ of the four segmentation classes. For example, the class (background, axon) means that in frame t_i, the pixel was classified as background while in frame t_{i+1}, it was an axon pixel. For T time steps, we therefore computed T-1 histograms. Additionally, we normalized each histogram to sum up to 1:

$$H(t_i, (c_1, c_2)) := H_0(t_i, (c_1, c_2)) \ / \ \sum_{a,b} H_0(t_i, (a, b))$$

Note that, the histograms were computed over small patches (height and width < 90 pixels) during training and during inference on windows of size 32x32 pixels.

537 We used an encoder-decoder RNN with attention[45]. The encoder f_{enc} consisted of a gated

538 recurrent unit (GRU) that obtained the histogram time sequence H as input. The encoder

539 computed the hidden representation of the histograms:

540 $$V = f_{enc}(H); V \in \mathbb{R}^{T \ x \ d}, H \in \mathbb{R}^{T \ x \ 16}$$

541 For our purpose, we used an architecture that was able to base the decision for a degeneration

542 class on the previous class predictions. To this end, the output $\vec{o}_i$ was computed iteratively in

543 C+1 steps as a sum of the previous output and the output of the decoder f_{dec}:

544 $$\vec{o}_i = \vec{o}_{i-1} + f_{dec}(\sigma(\vec{o}_{i-1}), \vec{s}_{i-1}); \vec{o} \in \mathbb{R}^C, \vec{s}_{i-1} \in \mathbb{R}^d$$

545 $$f_{dec}(\sigma(\vec{o}_{i-1}), \vec{s}_{i-1}) = W_{out}\vec{z}_i; \ W_{out} \in \mathbb{R}^{C \ x \ d}$$

546 C is the number of degeneration classes (4) and d is the hidden dimension (we used 256); $i =$

547 $1,\dots,C + 1$. σ is the sigmoid function. The decoder employed a GRU that depended on the

548 context vector $\vec{c}_i$ and the hidden state vector $\vec{s}_{i-1}$:

549 $$\vec{z}_i, \vec{s}_i = GRU(\vec{c}_i, \vec{s}_{i-1}); \ \vec{z}_i \in \mathbb{R}^d$$

550 The context vector is a weighted sum of the encoder representations. At each iteration, these

551 weights can change, enabling the network to focus on different time-steps. We assumed that a

552 specific pattern of degeneration happened only in a limited number of time frames that were

553 smaller than the whole input video. The weights depended on the current state of the decoder

554 and the current output:

555 $$\vec{c}_i = V^T \vec{\alpha}_i; \vec{\alpha}_i \in \mathbb{R}^T$$

556 $$\vec{\alpha}_i = Softmax(W_{att} [\vec{s}_{i-1}, ReLU(W_{in}\vec{o}_{i-1})]); \ W_{att} \in \mathbb{R}^{T \ x \ 2d}, W_{in} \in \mathbb{R}^{d \ x \ C}$$

557 Here, $[\vec{a}, \vec{b}]$ is the concatenation of two vectors. The final output y is normalized by the sigmoid

558 function:

559 $$y = \sigma(\vec{o}_{C+1}) \in [0,1]^C.$$

560 Apart from the weights used by the GRUs, W_{in}, W_{att}, and W_{out} are learnable weights.

561   The EntireAxon RNN was trained with 162 images for 60 epochs using the lamb optimizer[46]

562   with a batch size of 128. We used a learning rate of 0.01 that was reduced by a factor of ten

563   every 15 epochs and an additional weight decay of 0.0001. The two GRUs (encoder and

564   decoder) contained three layers, and we used dropout with a p-value of 0.9. To increase the

565   RNN robustness against varying axon thickness, we also added eroded versions of the

566   segmentation data using a cross-shape as kernel with the sizes three, five, and seven.

567   Accordingly, each image existed six times in the dataset: three eroded versions and three

568   unchanged copies, to keep a 50 % chance of having the original image for training.

569

570   **Ten-fold cross-validation of the RNN**

571   To validate the RNN, we used ten-fold cross-validation[47]. For the given 162 training images,

572   we determined ten separate test sets (nine sets containing 17 images and one set including nine

573   images) and, each time, trained with the remaining 145 (153) images as described above. Mean

574   recall, precision, and F1 score over the ten sets were determined as described above.

575

576   **Analysis of morphological pattern of AxD using the EntireAxon RNN**

577   All segmentations of AxD after hemin exposure were automatically analyzed with the trained

578   EntireAxon RNN, which predicted the occurrence of the four morphological patterns of AxD

579   in a pixel-wise manner. To note: A pixel can be predicted to belong to 0, 1 or multiple

580   morphological patterns. Only pixels previously identified as degenerated over time were

581   considered by applying a 'fragmentation mask' that included all no-background pixels that

582   changed to either background or fragment during the recording time.

583   For each experimental condition (i.e. hemin concentration), the percentage of the occurrence of

584   each morphological pattern was calculated as the sum of all pixels per morphological pattern

585   on all images of that experimental day divided by the 'fragmentation mask' as follows:

586      $'morphological\ pattern'[\%]$

587
$$= \frac{\sum pixel\ of\ morphological\ pattern_i}{\sum pixel\ no\ background \rightarrow background\ or\ fragment} * 100$$

588

589 **Statistical analysis**

590 Normality was evaluated with the Kolmogorov-Smirnov test, variance homogeneity using the

591 Levené test, and sphericity by the Mauchly test. When the data were normally distributed and

592 variance homogeneity was met, one-way ANOVA followed by the Bonferroni post hoc test

593 was performed. In case the data were not normally distributed, the Kruskal-Wallis test was

594 performed for multiple comparisons of independent groups followed by the post hoc Mann-

595 Whitney U test with α-correction according to Bonferroni to adjust for the inflation of type I

596 error due to multiple testing. For the repeated testing with covariates, a repeated measures

597 ANOVA was performed with Greenhouse-Geisser adjustment if sphericity was not given. Data

598 are represented as mean ± standard deviation (SD) except for the nonparametric data of the

599 AUC for axonal fragments as well as retraction and swelling degeneration, where medians are

600 given. A value of $p<0.05$ was considered statistically significant. For the Kruskal-Wallis test

601 followed by Mann-Whitney U, $p=0.05/k$ was used, with k as the number of single hypotheses.

602 K=3 for AUC analyses (comparison of three different concentrations of hemin vs. 0 µM hemin),

603 thus α=0.0167 was considered statistically significant. K=6 for swelling degeneration

604 (comparison of four different concentrations of hemin against each other), thus α=0.0083 was

605 considered statistically significant. The detailed statistical analyses can be found in the **suppl.**

606 **Tables 1-3**. All statistical analyses were performed with IBM SPSS version 23

607 (RRID:SCR_002865).

608

Acknowledgments

Author contributions

M.Z. designed the experiments. A. Palumbo, A. Pabst and M.Z. designed the device. A. Palumbo, A. Pabst, S.P., R.S., C.K., and N.K. carried out the fabrication of the device. S.K.L. performed the immunostaining of the somata and axons and analyzed the respective data. P.G. and A.M.M. developed the deep learning tool, P.G., L.H., and L.B. developed the algorithms to retrieve the output. A. Palumbo, S.K.L. and L.H. labeled the images for the deep learning training and validation. A. Palumbo and C.F. performed the time-lapse recordings of AxD. A. Palumbo conducted the live cell imaging, the determination of the morphological patterns of AxD and analyzed the data for the respective experiments. A. Palumbo, P.G., A.M.M., J.B., and M.Z. discussed and interpreted the data. M.Z. performed the statistical analysis. A. Palumbo, M.I. and M.Z. performed the graphical artwork. A. Palumbo, P.G., and M.Z wrote the manuscript. All authors discussed and commented on the final version of the manuscript.

Competing interest statement

A. Palumbo, P.G., and M.Z. declare that they have filed a patent for the microfluidic device and the EntireAxon deep learning algorithm to quantify axonal degeneration (European Patent Office, file number: 20152016.0, in revision). All other authors declare no conflict of interest.

Data availability

The data and code are available upon reasonable request to the corresponding authors.

References

1.   Luo, L. & O'Leary, D. D. M. Axon Retraction and Degeneration in Development and Disease. *Annu. Rev. Neurosci.* **28**, 127–156 (2005).

2.   Lingor, P., Koch, J. C., Tönges, L. & Bähr, M. Axonal degeneration as a therapeutic target in the CNS. *Cell Tissue Res* **349**, 289–311 (2012).

3.   Salvadores, N., Sanhueza, M., Manque, P. & Court, F. A. Axonal Degeneration during Aging and Its Functional Role in Neurodegenerative Disorders. *Front. Neurosci.* **11**, 451 (2017).

4.   Pease, S. E. & Segal, R. A. Preserve and protect: maintaining axons within functional circuits. *Trends in Neurosciences* **37**, 572–582 (2014).

5.   Neukomm, L. J. & Freeman, M. R. Diverse cellular and molecular modes of axon degeneration. *Trends in Cell Biology* **24**, 515–523 (2014).

6.   Bishop, D. L., Misgeld, T., Walsh, M. K., Gan, W.-B. & Lichtman, J. W. Axon Branch Removal at Developing Synapses by Axosome Shedding. *Neuron* **44**, 651–661 (2004).

7.   Cavanagh, J. B. The 'dying back' process. A common denominator in many naturally occurring and toxic neuropathies. *Arch. Pathol. Lab. Med.* **103**, 659–664 (1979).

8.   Coleman, M. P. Axon degeneration mechanisms: commonality amid diversity. *Nat Rev Neurosci* **6**, 889–898 (2005).

9.   Beirowski, B. *et al.* The progressive nature of Wallerian degeneration in wild-type and slow Wallerian degeneration (WldS) nerves. *BMC Neurosci* **6**, 6 (2005).

10.   Nikić, I. *et al.* A reversible form of axon damage in experimental autoimmune encephalomyelitis and multiple sclerosis. *Nat Med* **17**, 495–499 (2011).

11.   Yong, Y. *et al.* p75NTR and DR6 Regulate Distinct Phases of Axon Degeneration Demarcated by Spheroid Rupture. *J. Neurosci.* **39**, 9503–9520 (2019).

12.   Saxena, S. & Caroni, P. Mechanisms of axon degeneration: From development to disease. *Progress in Neurobiology* **83**, 174–191 (2007).

13.   Wang, J. T., Medress, Z. A. & Barres, B. A. Axon degeneration: Molecular mechanisms of a self-destruction pathway. *J Cell Biol* **196**, 7–18 (2012).

14.   Sasaki, Y., Vohra, B. P. S., Lund, F. E. & Milbrandt, J. Nicotinamide Mononucleotide Adenylyl Transferase-Mediated Axonal Protection Requires Enzymatic Activity But Not Increased Levels of Neuronal Nicotinamide Adenine Dinucleotide. *Journal of Neuroscience* **29**, 5525–5535 (2009).

15.   Becker, T. & Madany, A. Morphology-based Features for Adaptive Mitosis Detection of In Vitro Stem Cell Tracking Data. *Methods Inf Med* **51**, 449–456 (2012).

16.   Pool, M., Thiemann, J., Bar-Or, A. & Fournier, A. E. NeuriteTracer: A novel ImageJ plugin for automated quantification of neurite outgrowth. *Journal of Neuroscience Methods* **168**, 134–139 (2008).

17.   Ho, S.-Y. *et al.* NeurphologyJ: An automatic neuronal morphology quantification method and its application in pharmacological discovery. *BMC Bioinformatics* **12**, 230 (2011).

18.   Li, Y. *et al.* AxonQuant: A Microfluidic Chamber Culture-Coupled Algorithm That Allows High-Throughput Quantification of Axonal Damage. *Neurosignals* **22**, 14–29 (2014).

19.   Campenot, R. B. Development of sympathetic neurons in compartmentalized cultures. *Developmental Biology* **93**, 13–21 (1982).

20.   Park, J. W., Vahidi, B., Taylor, A. M., Rhee, S. W. & Jeon, N. L. Microfluidic culture platform for neuroscience research. *Nat Protoc* **1**, 2128–2136 (2006).

21.   Dehmelt, L. & Halpain, S. The MAP2/Tau family of microtubule-associated proteins. *Genome Biol* **6**, 204 (2004).

22.   Wiedenmann, B. & Franke, W. W. Identification and localization of synaptophysin, an

683   integral membrane glycoprotein of Mr 38,000 characteristic of presynaptic vesicles. *Cell* **41**,
684   1017–1028 (1985).

685   23.   Ronneberger, O., Fischer, P. & Brox, T. U-Net: Convolutional Networks for
686   Biomedical Image Segmentation. Preprint at https://arxiv.org/abs/1505.04597 (2015).

687   24.   He, K., Zhang, X., Ren, S. & Sun, J. Deep Residual Learning for Image Recognition.
688   Preprint at https://arxiv.org/abs/1512.03385 (2015).

689   25.   Dietterich, T. G. Ensemble Methods in Machine Learning. in *Multiple Classifier*
690   *Systems* vol. 1857 1–15 (Springer Berlin Heidelberg, 2000).

691   26.   Huang, H.-K. *et al.* Mixture of deep CNN-based ensemble model for image retrieval.
692   in *2016 IEEE 5th Global Conference on Consumer Electronics* 1–2 (IEEE, 2016).
693   doi:10.1109/GCCE.2016.7800375.

694   27.   Vuola, A. O., Akram, S. U. & Kannala, J. Mask-RCNN and U-Net Ensembled for
695   Nuclei Segmentation. in *2019 IEEE 16th International Symposium on Biomedical Imaging*
696   *(ISBI 2019)* 208–212 (IEEE, 2019). doi:10.1109/ISBI.2019.8759574.

697   28.   Zille, M. *et al.* Neuronal Death After Hemorrhagic Stroke In Vitro and In Vivo Shares
698   Features of Ferroptosis and Necroptosis. *Stroke* **48**, 1033–1043 (2017).

699   29.   Cui, Y. *et al.* Axonal degeneration in an in vitro model of ischemic white matter
700   injury. *Neurobiology of Disease* **134**, 104672 (2020).

701   30.   Venkatasubramanian, C. *et al.* Natural History and Prognostic Value of Corticospinal
702   Tract Wallerian Degeneration in Intracerebral Hemorrhage. *JAHA* **2**, (2013).

703   31.   Tao, C., Hu, X., Li, H. & You, C. White Matter Injury after Intracerebral Hemorrhage:
704   Pathophysiology and Therapeutic Strategies. *Front. Hum. Neurosci.* **11**, 422 (2017).

705   32.   Chen, X. *et al.* The Impact of Intracerebral Hemorrhage on the Progression of White
706   Matter Hyperintensity. *Front. Hum. Neurosci.* **12**, 471 (2018).

707   33.   Hemorrhagic Stroke Academia Industry (HEADS) Roundtable Participants. Basic and
708   Translational Research in Intracerebral Hemorrhage: Limitations, Priorities, and
709   Recommendations. *Stroke* **49**, 1308–1314 (2018).

710   34.   Nikolaev, A., McLaughlin, T., O'Leary, D. D. M. & Tessier-Lavigne, M. APP binds
711   DR6 to trigger axon pruning and neuron death via distinct caspases. *Nature* **457**, 981–989
712   (2009).

713   35.   Maor-Nof, M. *et al.* Axonal Degeneration Is Regulated by a Transcriptional Program
714   that Coordinates Expression of Pro- and Anti-degenerative Factors. *Neuron* **92**, 991–1006
715   (2016).

716   36.   Pease-Raissi, S. E. *et al.* Paclitaxel Reduces Axonal Bclw to Initiate IP3R1-Dependent
717   Axon Degeneration. *Neuron* **96**, 373-386.e6 (2017).

718   37.   Tang-Schomer, M. D., Johnson, V. E., Baas, P. W., Stewart, W. & Smith, D. H.
719   Partial interruption of axonal transport due to microtubule breakage accounts for the
720   formation of periodic varicosities after traumatic axonal injury. *Experimental Neurology* **233**,
721   364–372 (2012).

722   38.   Van Laar, V., Arnold, B. & Berman, S. Primary Embryonic Rat Cortical Neuronal
723   Culture and Chronic Rotenone Treatment in Microfluidic Culture Devices. *BIO-PROTOCOL*
724   **9**, (2019).

725   39.   Hosmane, S., Yang, I. H., Ruffin, A., Thakor, N. & Venkatesan, A. Circular
726   compartmentalized microfluidic platform: Study of axon–glia interactions. *Lab Chip* **10**, 741
727   (2010).

728   40.   Biffi, E. *Microfluidic and Compartmentalized Platforms for Neurobiological*
729   *Research*. (2015).

730   41.   Grüning, P., Palumbo, A., Zille, M., Barth, E. & Madany Mamlouk, Amir. A task-
731   dependent active learning method for axon segmentation with CNNs. *Proc AUTOMED* **1**,
732   (2020).

733   42.   Deng, J. *et al.* ImageNet: A large-scale hierarchical image database. in *2009 IEEE*

734   *Conference on Computer Vision and Pattern Recognition* 248–255 (IEEE, 2009).
735   doi:10.1109/CVPR.2009.5206848.
736   43.   Forman, G. & Scholz, M. Apples-to-apples in cross-validation studies: pitfalls in
737   classifier performance measurement. *SIGKDD Explor. Newsl.* **12**, 49 (2010).
738   44.   Lowe, D. G. Distinctive Image Features from Scale-Invariant Keypoints. *International*
739   *Journal of Computer Vision* **60**, 91–110 (2004).
740   45.   Bahdanau, D., Cho, K. & Bengio, Y. Neural Machine Translation by Jointly Learning
741   to Align and Translate. Preprint at https://arxiv.org/abs/1409.0473 (2016).
742   46.   You, Y. *et al.* Large Batch Optimization for Deep Learning: Training BERT in 76
743   minutes. Preprint at https://arxiv.org/abs/1904.00962 (2020).
744   47.   Hastie, T., Tibshirani, R. & Friedman, J. *The Elements of Statistical Learning*.
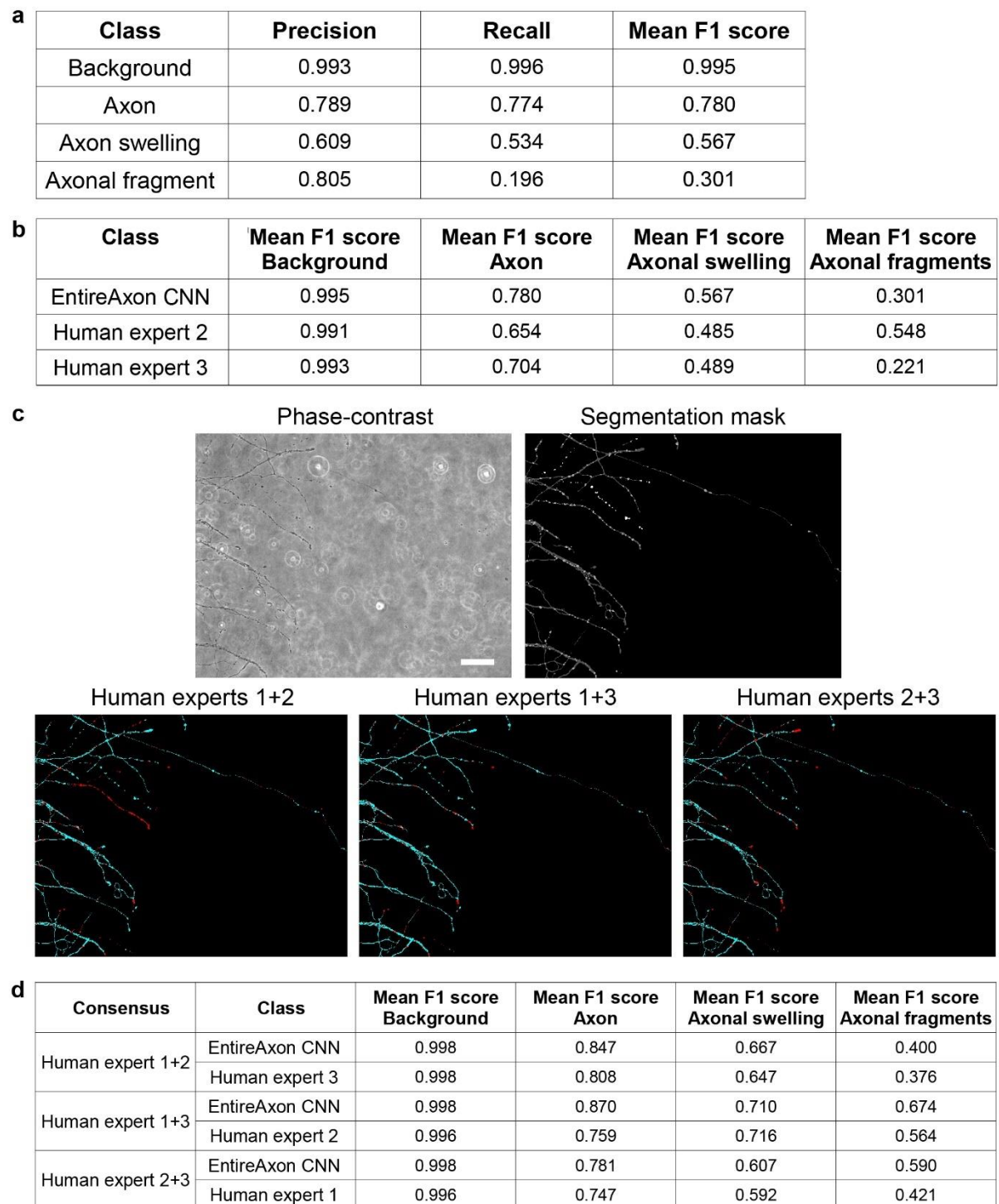745   (Springer New York, 2009). doi:10.1007/978-0-387-84858-7.
746

Figures
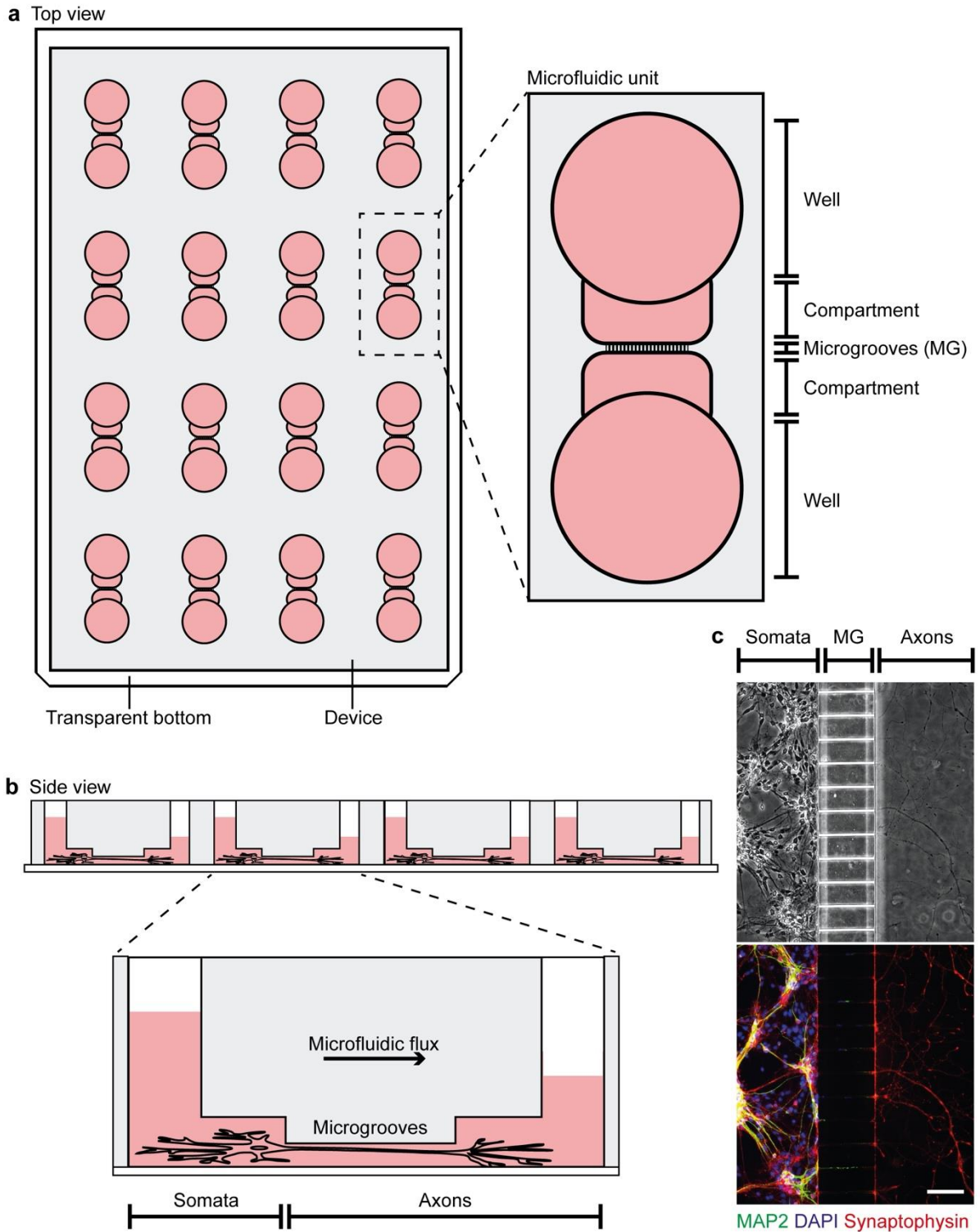
Fig. 1 Microfluidic device for the high-throughput cultivation of axons. a, The microfluidic device incorporates 16 individual microfluidic units for axon cultivation. One microfluidic unit consists of two wells that are connected through compartments and microgrooves (MG). **b**, Primary cortical neurons are seeded into the soma compartment from which their axons grow through the MG into the axon compartment. Directed growth is supported by culture medium microflux due to different medium volumes between the two wells. **c**, Phase-contrast image of axons that were spatially separated from their somata by the MG at *day in vitro* 7, which we confirmed by immunofluorescence staining of dendrites using microtubule-associated protein 2 (MAP2, green) and axons using synaptophysin (red). DAPI (blue) was used for nuclear counterstaining (top). Scalebar, 100 µm.
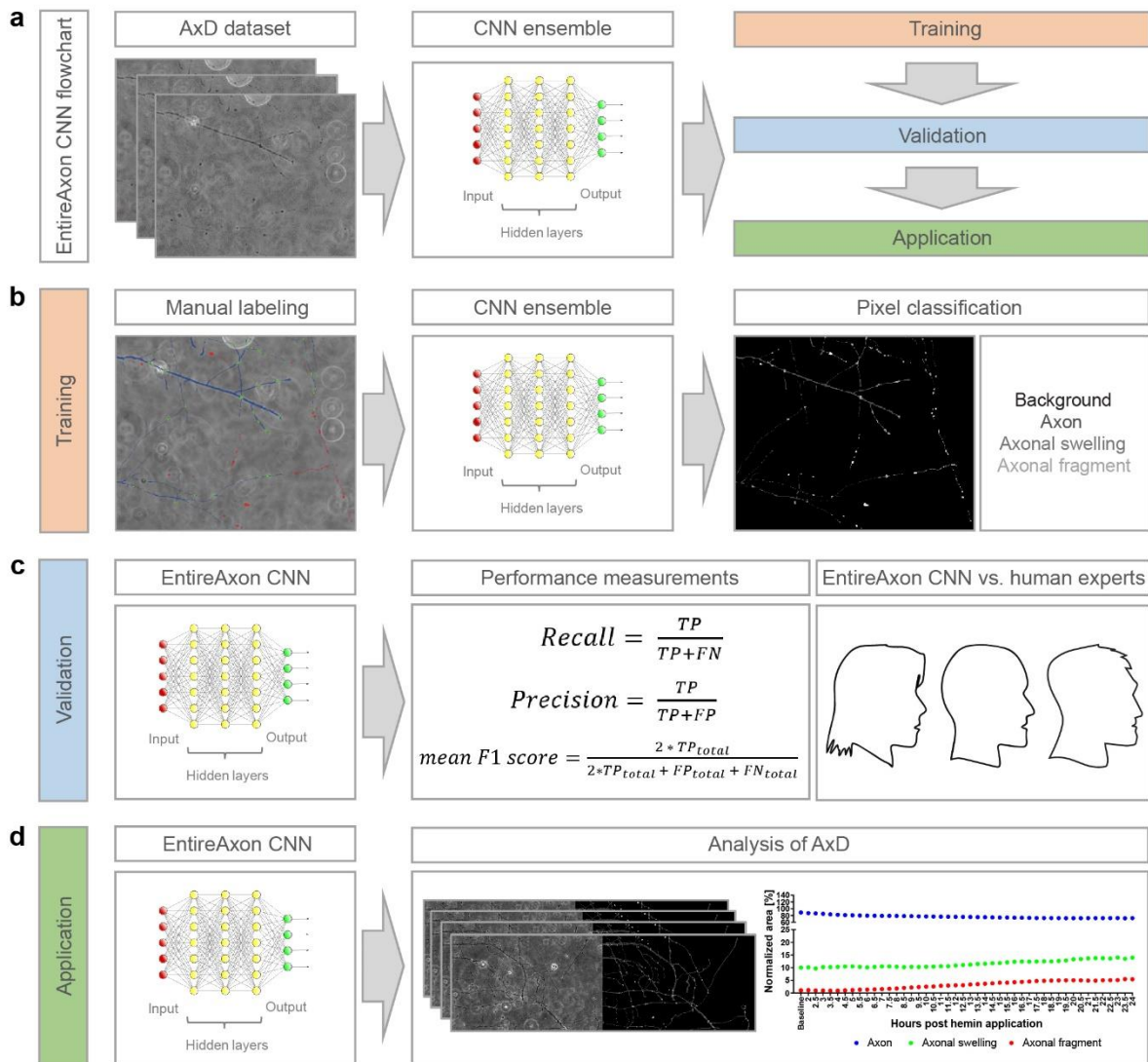
758
759 **Fig. 2 EntireAxon convolutional neural network (CNN) for the high-throughput analysis of axonal degeneration (AxD).**
760 **a,** The flow chart of the EntireAxon CNN. The AxD data was separated into training, validation, and testing data. **b,** We
761 manually labeled the training data to segment each pixel into the four classes 'background', 'axon', 'axonal swelling', and
762 'axonal fragment', which are displayed in the output image in black, dark grey, intermediate grey, and light grey, respectively.
763 We trained an ensemble comprising 8 CNNs to segment the four classes. **c,** The EntireAxon CNN was validated with a separate
764 validation dataset to assess its performance (recall, precision, and mean F1 score), which was compared to human experts. **d,**
765 The EntireAxon CNN was applied to data on AxD induced by the exposure of hemin, which is used to model of hemorrhagic
766 stroke *in vitro*.
767

a

Class	Precision	Recall	Mean F1 score
Background	0.993	0.996	0.995
Axon	0.789	0.774	0.780
Axon swelling	0.609	0.534	0.567
Axonal fragment	0.805	0.196	0.301

b

Class	Mean F1 score Background	Mean F1 score Axon	Mean F1 score Axonal swelling	Mean F1 score Axonal fragments
EntireAxon CNN	0.995	0.780	0.567	0.301
Human expert 2	0.991	0.654	0.485	0.548
Human expert 3	0.993	0.704	0.489	0.221

c

d

| Consensus	Class	Mean F1 score Background	Mean F1 score Axon	Mean F1 score Axonal swelling	Mean F1 score Axonal fragments
Human expert 1+2	EntireAxon CNN	0.998	0.847	0.667	0.400
	Human expert 3	0.998	0.808	0.647	0.376
Human expert 1+3	EntireAxon CNN	0.998	0.870	0.710	0.674
	Human expert 2	0.996	0.759	0.716	0.564
Human expert 2+3	EntireAxon CNN	0.998	0.781	0.607	0.590
	Human expert 1	0.996	0.747	0.592	0.421

768

Fig. 3 The EntireAxon convolutional neural network (CNN) sensitively and specifically recognizes features of axonal degeneration (AxD). a, Validation of the EntireAxon CNN performance for all four classes 'background', 'axon', 'axonal swelling' and 'axonal fragment' in before unseen phase-contrast microscopic images. **b**, Comparison of the mean F1 scores between the EntireAxon CNN and two human experts on the ground truth (human expert 1 who also labeled the training images) to recognize background, axon, axonal swelling and axonal fragments. **c**, Phase-contrast validation image, its EntireAxon CNN segmentation mask, and the consensus labeling masks of two human experts that show the overlap (cyan) or difference (red) between the labels. Scalebar, 100 µm. **d**, Comparison of the mean F1 scores between the EntireAxon CNN and the human expert on the consensus labeling of the other two human experts.
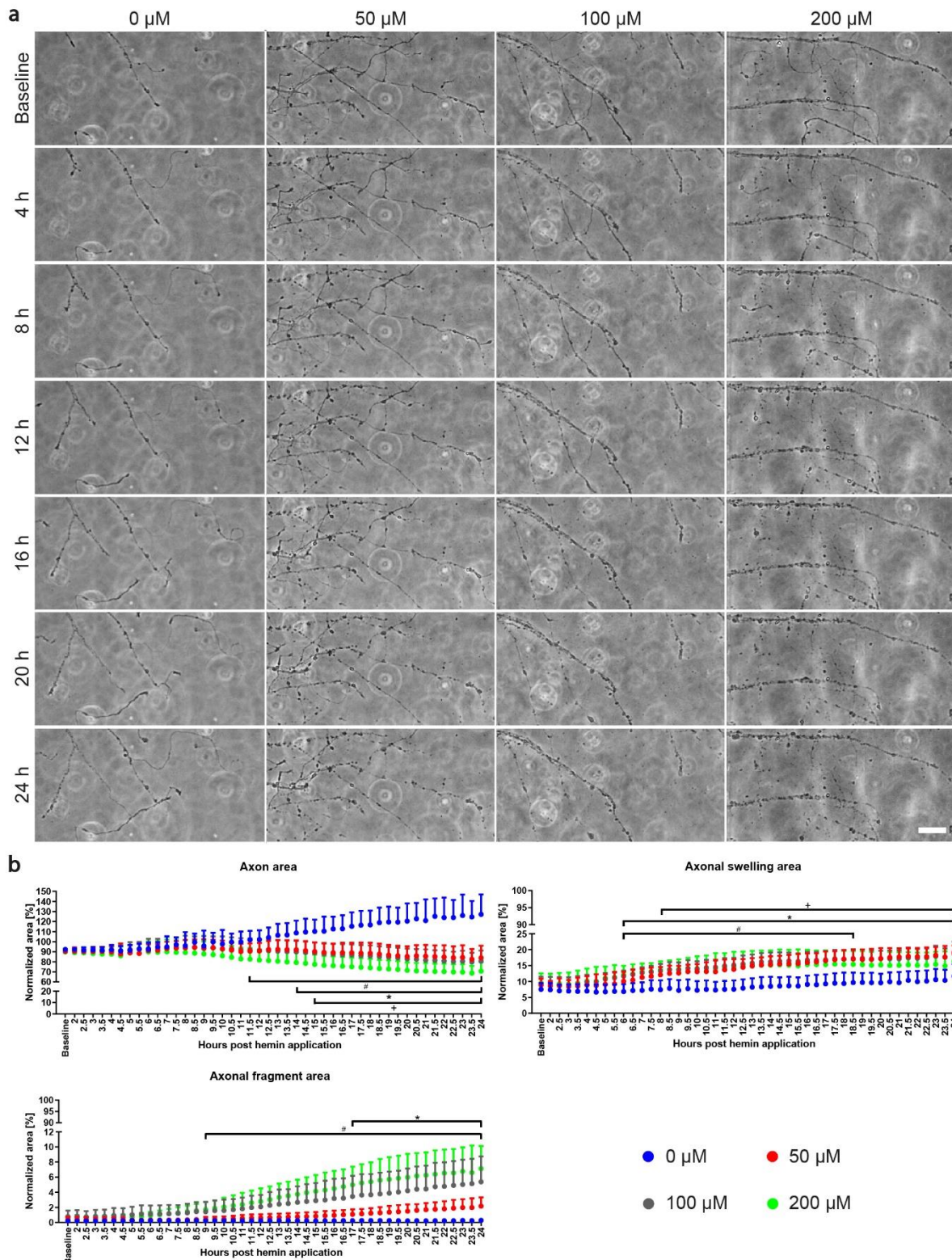
777

Fig. 4 Hemin-induced axonal degeneration (AxD) progresses time- and concentration-dependently. a, Axons treated with hemin (50, 100, 200 µM) degenerated compared to vehicle-treated axons (0 µM) that continued to grow. Scalebar, 50 µm. For complete time-lapse videos including segmentation, refer to **suppl. Videos 1-4**. **b**, Quantification of AxD over 24 hours in phase-contrast images. For AUC analyses, please refer to **suppl. Fig. 2**. To determine the time course, the sum of pixels in each class and hemin concentration over time was normalized to the baseline of that class and condition. The quantification of the phase-contrast images over 24 hours revealed significantly smaller axon areas starting at 11.5 hours (200 µM), 14 hours (100 µM), and 15 hours (50 µM) after hemin treatment compared to control (0 µM). The axonal fragment area significantly increased from 9.5 hours onwards (200 µM vs. 0 µM) and from 17.5 hours (100 µM vs. 0 µM), while the axonal swelling area increased from 6 hours onwards (100-200 µM) and from 8 hours (50 µM). n=6 independent cultures of primary cortical

788   neurons. Means ± SD are given. +, *, # p < 0.05; + = 50 µM vs. 0 µM, * = 100 µM vs. 0 µM, # = 200 µM vs. 0 µM. For exact
789   *p* values, refer to **suppl. Tab. 1**.
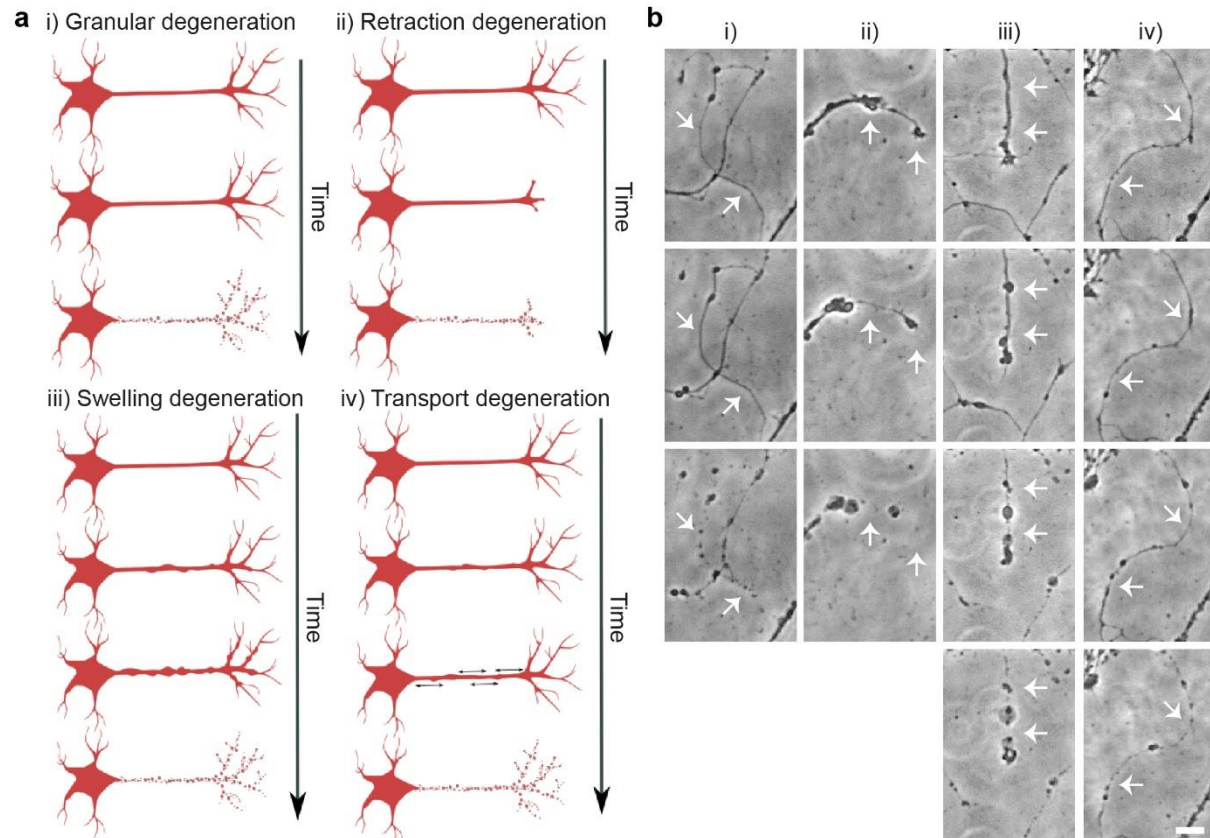
Fig. 5 Axonal degeneration (AxD) is a morphologically heterogeneous process. **a**, Schematic overview of the proposed AxD morphological patterns: i) granular degeneration, ii) retraction degeneration, iii) swelling degeneration, and iv) transport degeneration. **b**, Phase-contrast recordings of the four different morphological patterns of AxD. Granular degeneration (i) is characterized by the fragmentation of the axon (white arrows). During retraction degeneration (ii), the axonal growth cone retracts in the proximal direction and the part of the axon in proximity of the growth cone disintegrates accompanied by axonal swellings (white arrows). During swelling degeneration (iii), many axonal swellings enlarge resulting in axonal fragments (white arrows). During transport degeneration (iv), axonal swellings are transported along the axon prior to the degeneration of the axon (white arrows). Scalebar, 20 µm. For complete time-lapse videos including segmentation, refer to **suppl. Videos 5-8.**
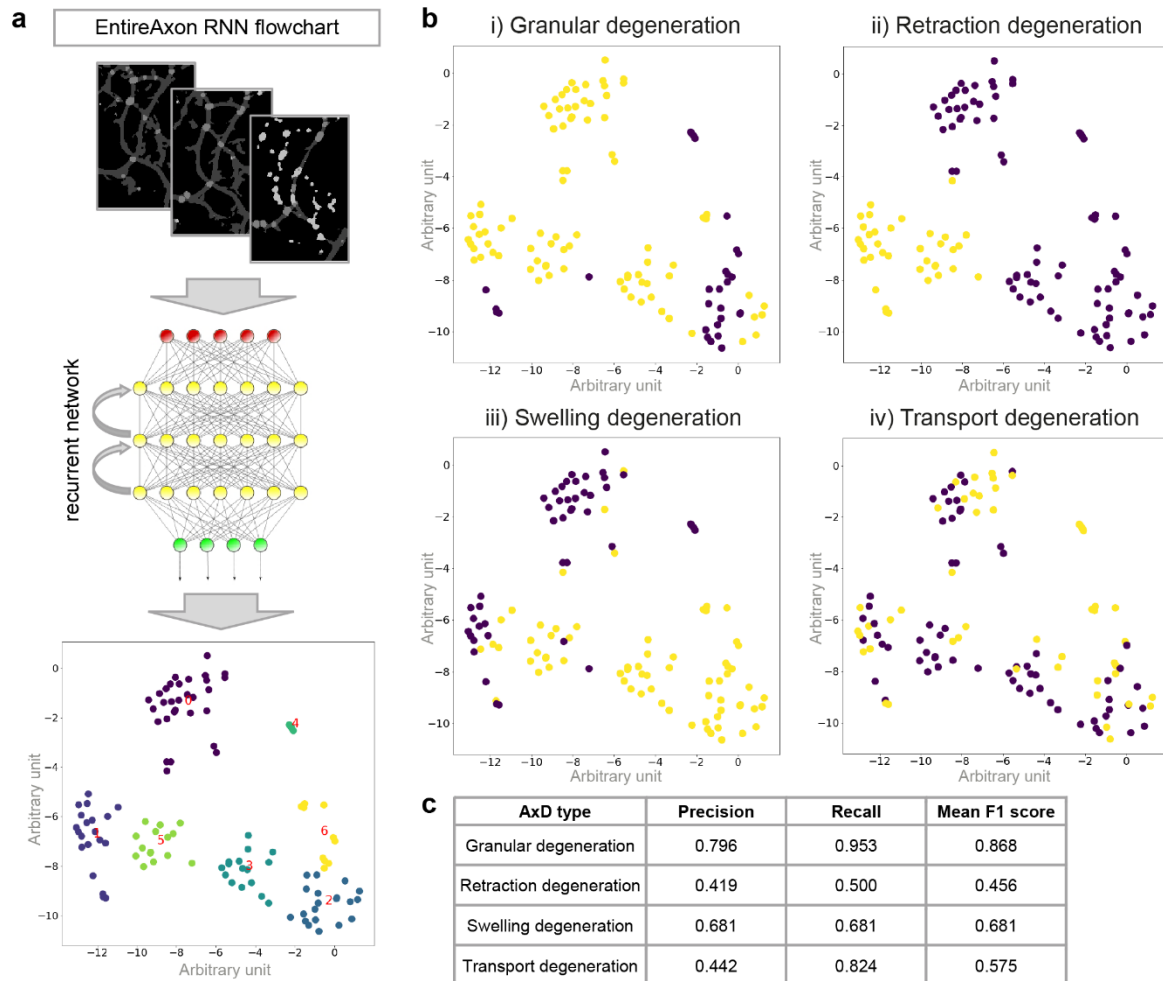
Fig. 6 The EntireAxon RNN deciphers four distinct patterns of axonal degeneration (AxD). **a,** Schematic workflow of recurrent neural network (RNN) to recognize and quantify morphological patterns of AxD based on the identification of seven clusters. The EntireAxon CNN segmentation masks were used for the RNN training, which determined the change in class over time. Based on the 16 different possible class changes, the RNN determined seven clusters (cluster 0-6). **b**, The clusters classify the four different morphological patterns of AxD with yellow indicating included and purple indicating excluded clusters: i) granular, ii) retraction, iii) swelling, and iv) transport degeneration. Clusters of granular degeneration overlap with recognized clusters of other morphological patterns (retraction, swelling, and transport degeneration). For more details on the morphological changes underlying the cluster analysis, refer to **Suppl. Fig. 4**. **c**, 10-fold cross-validation of the four morphological patterns of AxD.

37
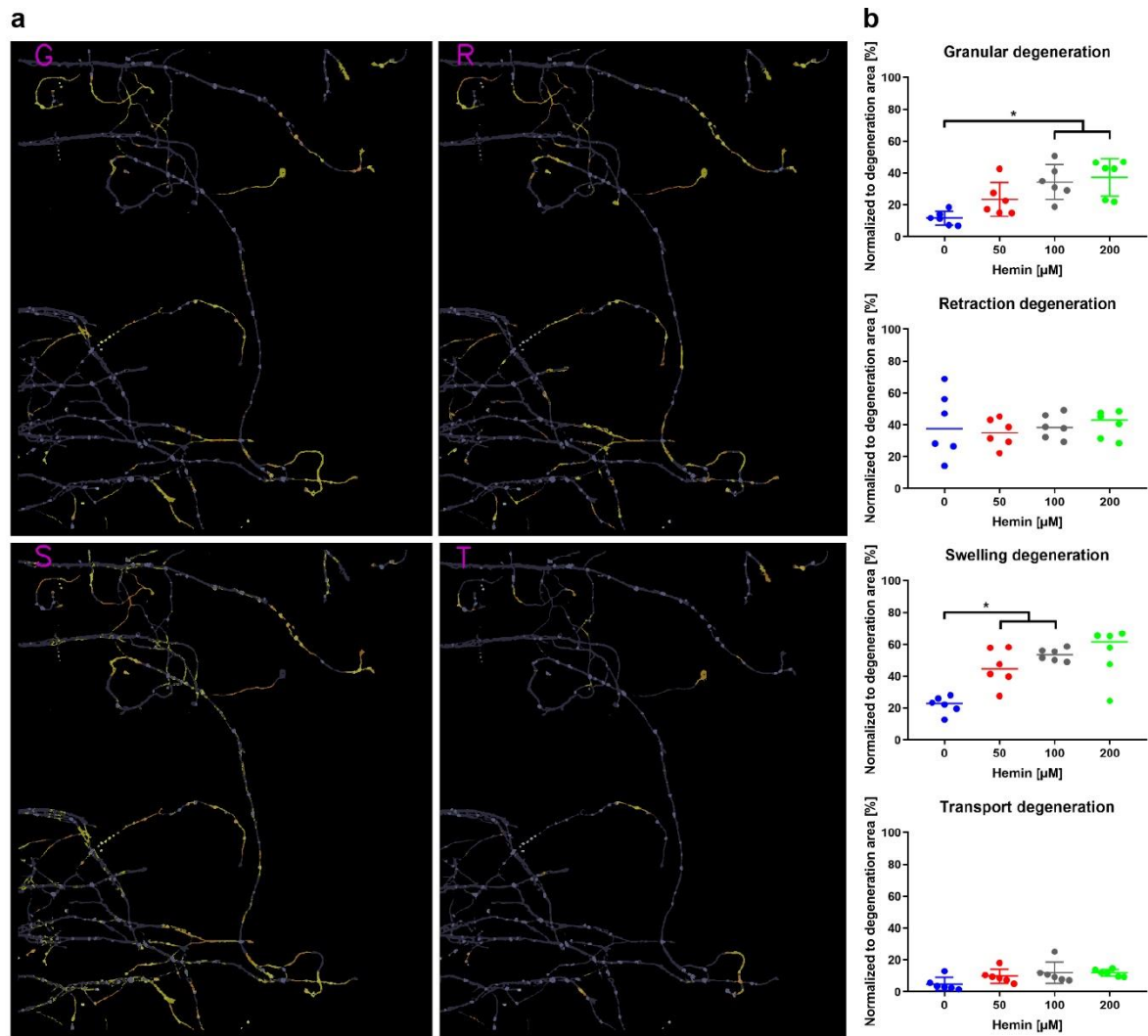
Fig. 7 Hemin induces concentration-dependent differences in the morphological patterns of axonal degeneration (AxD). **a**, The classification of granular (G), retraction (R), swelling (S), and transport degeneration (T) in axons treated with 200 µM hemin. Scalebar, 100 µm. For the complete time-lapse video including segmentation, refer to **suppl. Videos 9. b**, Quantification of the four morphological patterns of AxD in hemin-induced AxD. n=6 independent cultures of primary cortical neurons. Means ± SD are given for granular and transport degeneration and, medians are given for retraction and swelling degeneration. * $p < 0.05$ vs. 0 µM for granular degeneration, * $p < 0.0083$ vs. 0 µM for swelling degeneration due to manual Bonferroni correction for nonparametric data. For exact p values, refer to **suppl. Tab. 3**.